Check for updates

ChemSusChem

Chemistry Europe
European Chemical Societies Publishing
ChemSusChem

RESEARCH ARTICLE

Large Language Model-Assisted Additive Selection for Synergistic Defect and Crystallization Control in Efficient Inverted Perovskite Solar Cells

Zhirui Chen[1] | Xinde Wang[2] | Jiaqi Wang[1] | Youcai Hu[3] | Huiji Hu[4,5] | Junyu Nie[1] | Ziyue Jiao[1] | Yi Wang[1] | Qi Li[3] | Zhihai Cheng[4,5] | Ze-Feng Gao[2] | Zhong-Yi Lu[2] | Cheng Mu[1]

[1]Key Laboratory of Advanced Light Conversion Materials and Biophotonics, Department of Chemistry, School of Chemistry and Life Resources, Renmin University of China, Beijing, P. R. China | [2]School of Physics, Renmin University of China, Beijing, P. R. China | [3]College of Chemistry and Molecular Engineering, Peking University, Beijing, P. R. China | [4]Key Laboratory of Quantum State Construction and Manipulation (Ministry of Education), School of Physics, Renmin University of China, Beijing, P. R. China | [5]Beijing Key Laboratory of Optoelectronic Functional Materials & Micro-nano Devices, School of Physics, Renmin University of China, Beijing, P. R. China

Correspondence: Ze-Feng Gao (zfgao@ruc.edu.cn) | Zhong-Yi Lu (zlu@ruc.edu.cn) | Cheng Mu (cmu@ruc.edu.cn)

Received: 11 November 2025 | **Revised:** 11 December 2025 | **Accepted:** 22 December 2025

Keywords: additives | crystallization control | large language model | perovskite solar cells

ABSTRACT

Precursor additives are crucial for enhancing the efficiency and stability of perovskite solar cells. However, their traditional selection of additives primarily relies on empirical trial-and-error approaches, which are time-consuming and inefficient. Herein, we utilize Perovskite-R1, a large language model, to rapidly identify an efficient additive: ethyl 2-aminopropanoate hydrochloride (EAH). This additive simultaneously passivates defects and regulates crystallization through the coordination of its –C═O and $-NH_3^+$ groups with the uncoordinated Pb^{2+} and I^- ions in the perovskite. These interactions significantly improve charge-carrier transport and suppress nonradiative recombination, leading to a champion power conversion efficiency (PCE) of 22.58%. Furthermore, the EAH-modified device exhibits excellent long-term stability, maintaining 95.1% and 94.1% of its initial PCE after 1368 h of storage in N_2 and 1272 h of thermal aging at 65°C, respectively. This study highlights the potential of integrating artificial intelligence with materials design to accelerate the discovery of high-performance, stable, and sustainable perovskite optoelectronic materials.

1 | Introduction

Perovskite solar cells (PSCs), owing to their outstanding optical and electronic properties, have emerged as promising candidates for next-generation photovoltaics technologies [1–7]. Since their first report in 2009, the power conversion efficiency (PCE) of PSCs has impressively increased from 3.8% to 27% [8, 9]. Despite these advancements, controlling the crystallization kinetics of perovskite films remains a major challenge. Rapid and uncontrolled crystallization often leads to surface roughness, pinhole formation, and small grain sizes [10], which increase the number of grain boundaries (GBs) and defects. These defects, particularly undercoordinated Pb^{2+} and iodine vacancies, induce nonradiative recombination and elevate trap-state densities, thereby hindering further improvements in device performance and stability [11, 12]. Therefore, regulating the crystallization dynamics of the perovskite layer and simultaneously passivating defects are pivotal to achieving high-performance and stable PSCs [13, 14].

Additive engineering has demonstrated highly effectiveness in addressing these issues by regulating perovskite crystallization and passivating defects [15–18]. For example, Li et al. introduced 4-chlorobenzylamine hydroiodide (4-CBAI) into the perovskite precursor, which promoted (001)-oriented crystallization, reduced surface roughness, and passivated trap states through coordination of –Cl to Pb^{2+} and $-NH_3^+$ to I^- [19]. Zhang et al. employed 4-fluorobenzenesulfonamide (4-FBSO) as

Zhirui Chen and Xinde Wang contributed equally to this work.

© 2026 Wiley-VCH GmbH.

an additive, whose terminal groups formed coordinate covalent bonds with Pb^{2+} ions, effectively retarding crystallization and yielding larger perovskite grains exceeding 1 μm [20]. Yi et al. utilized a chlorine-substituted aromatic polycyclic derivative (BNCl) to promote preferential perovskite crystallization and passivate surface and GB defects through strong interaction with both lead iodide and dimethyl sulfoxide [21]. Liu et al. employed the multifunctional piperazinium bromide molecules to passivate defects, enabling the ultimate quality improvement of 2.03 eV perovskite films via increased grain size and suppressed phase segregation [22]. Zhang group introduced ammonium hexachlorostannate (AH) via a room-temperature aqueous coating method to achieve defect passivation and crystallinity enhancement, thereby boosting charge extraction and suppressing nonradiative recombination, which improved device efficiency and stability [23]. However, conventional additive development still relies heavily on extensive trial-and-error processes, which require considerable time and resources to evaluate candidate additives, which greatly limits the progress of PSC optimization [24].

Artificial intelligence (AI) has fundamentally reshaped the landscape of materials science, driving a paradigm shift toward data-driven exploration and accelerating materials discovery through AI-driven inverse design. Advanced deep learning architectures have achieved significant breakthroughs in both property prediction and inverse design [25–28]. For instance, graph neural networks (GNNs) have revolutionized the prediction of material properties by effectively capturing complex atomic interactions and topological structures [29], while generative models like crystal diffusion variational autoencoders (CDVAE) have demonstrated remarkable success in the inverse design of novel crystal structures with targeted functionalities. Complementing these structure-based models, the recent emergence of large language models (LLMs) represents another major stride in the field. LLMs demonstrate immense potential not only in processing vast unstructured chemical data and assisting in complex chemical reasoning [30–32], but also in the generative design of molecules and crystals by treating chemical structures as language sequences [33, 34], having shown great promise in learning correlations between chemical structures and functional properties from scientific literature [35]. Such models can provide intelligent and systematic guidance for additive design and screening, offering a powerful new strategy for enhancing PSC performance.

In this work, we utilized Perovskite-R1 [36], a domain-specific LLM trained by our team on a curated dataset based on the Qwen3-32B architecture. This model was capable of providing expert recommendations for PSC precursor additives. By establishing a workflow of dataset construction, model training, additive screening, and experimental validation, we identified ethyl 2-aminopropanoate hydrochloride (EAH) as a high-performance additive. The –C═O and $–NH_3^+$ groups in the EAH coordinated with uncoordinated Pb^{2+} and I^- ions, thereby stabilizing the perovskite structure and suppressing ion migration. This coordination interaction suppressed defect formation and delayed crystallization during annealing, resulting in a smoother surface with fewer defects. Consequently, the EAH-treated PSC achieved a PCE of 22.58%, along with a significantly reduced defect density and improved charge-transport carrier behavior. Moreover, this optimized device exhibited remarkable stability, retaining 95.1% of its initial PCE after 1368 h of storage in N_2 and 94.1% after 1272 h of thermal aging at 65°C.

2 | Results and Discussion

An inverted PSC with the structure of NiO_x/Me-4PACz/perovskite/C_{60}/BCP/Ag is shown in Figure 1a. Defects in perovskite film absorbers, notably anion vacancies and undercoordinated Pb^{2+}, promote nonradiative recombination, impede charge transport and extraction, and consequently limit optical and electronic performance of the device. To mitigate these issues, researchers introduce additives into the perovskite precursor solution to slow crystallization and to passivate the defects (Figure 1b) [37]. The relationship between additive chemical knowledge and target device properties can be learnt by an LLM workflow based on extensive literature and molecular data (Figure 1c). In steps I–II, we compiled 1,232 research articles on perovskite precursor additives and assembled a candidate molecular library containing 33,269 compounds to form a comprehensive database. Using the OpenAI o1 model, we converted the literature into question–answer pairs for instruction tuning, thereby generating a high-quality training dataset. This dataset was used to fine-tune the pretrained QWG-32B model, producing the domain-specific Perovskite-R1 model for additive screening and design. During stages III–IV, we input a prompt containing additive design criteria into the Perovskite-R1 LLM to screen for promising additive molecules: (1) noncovalent interactions, (2) additive-precursor coordination retards crystallization, and (3) synergistic multifunctional groups. Guided by this model, a simple and effective additive named EAH was identified and incorporated into the perovskite precursor to achieve defect passivation and controlled crystallization for efficient and stable PSCs.

The molecular structure of EAH is shown in Figure 2a. To elucidate the interaction mechanism between the –C═O and $–NH_3^+$ groups in EAH and the perovskite precursor, Fourier transform infrared (FTIR) spectroscopy was performed. As shown in Figure 2b, the N—H stretching vibration of $–NH_3^+$ shifted from 2984.68 cm^{-1} for pure EAH to 3130.21 cm^{-1} for EAH + FAI film, indicating the formation of the N—H···I hydrogen bond [19]. In Figure 2c, the characteristic –C═O peak shifted from 1742.34 cm^{-1} in the EAH film to 1735.90 cm^{-1} in the EAH + PbI_2 film, while the N—H shift was negligible (Figure S1). This suggested that the oxygen atom in EAH coordinates with Pb^{2+} through –C═O···Pb bonding, facilitated by the lone-pair electrons of the –C═O group [38]. Additionally, the FTIR spectrum of the EAH + FAI film (Figure S2) showed a further redshift of the –C═O vibration, confirming the possible formation of the –C═O···H—N hydrogen bond [39]. X-ray photoelectron spectroscopy (XPS) further confirmed these interactions. After EAH incorporation, the Pb 4f peaks shifted to lower binding energy (Figure 2d), indicating electron donation from the electronegative C═O group of EAH to undercoordinated Pb^{2+} ions. Similarly, the I 3d peak also shifted to lower binding energies (Figure 2e), indicating increased electron cloud density around Pb—I octahedra [40]. Quantitative XPS analysis revealed a higher I/Pb ratio (2.95) for the EAH-treated film compared with the pristine perovskite (2.54), indicating enhanced crystallinity and suppressed iodide ion migration due to EAH modification [41]. The XPS characterization results strongly corroborate that EAH molecules utilize carbonyl and amino groups to effectively passivate defects in the bulk phase, thereby enhancing PSCs performance. Figure 2f showed a schematic illustrating the defect-passivation mechanism by the EAH.

1864564x, 2026, 3, Downloaded from https://chemistry-europe.onlinelibrary.wiley.com/doi/10.1002/cssc.202502563 by RENMIN UNIVERSITY OF CHINA NON-EAL ACCOUNT, Wiley Online Library on [04/11/2026]. See the Terms and Conditions (https://onlinelibrary.wiley.com/terms-and-conditions) on Wiley Online Library for rules of use; OA articles are governed by the applicable Creative Commons License

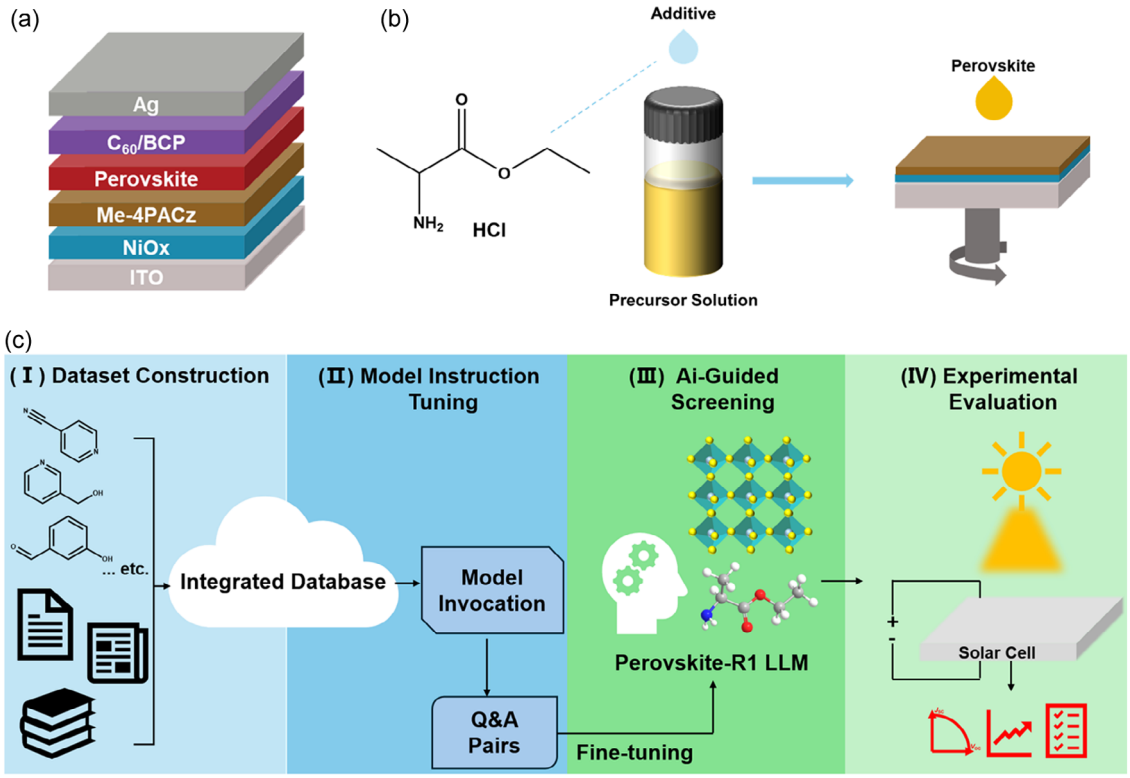


FIGURE 1 | (a) Schematic of the inverted PSC structure. (b) Device-fabrication process using incorporating. (c) Workflow for additive selection process assisted by Perovskite-R1 LLM.

The influence of EAH on the electronic structure of perovskite films was further investigated using ultraviolet photoelectron spectroscopy (UPS). From the secondary electron cutoff edge (E_{Cutoff}) and Fermi edge (E_{Fermi}) positions (Figure 2g,h), the work function (WF), conduction band minimum (CBM), and valence band maximum (VBM) were determined. Upon EAH treatment, the WF decreased from 4.86 to 4.81 eV, indicating that defect passivation shifted the Fermi energy level closer to the conduction band, rendering the material more n-type [42, 43]. As shown in the energy-level diagram in Figure 2i, EAH treatment optimized the energy-level alignment with the electron-transport layer and enhanced charge-extraction efficiency [44–46]. The optimization is primarily attributed to the effective passivation of Pb- and I-related defects in perovskite by EAH molecules through hydrogen bonding and coordination, which facilitated the alignment.

To elucidate the crystallization dynamics of perovskite film during the annealing stage, in situ UV–vis absorption spectroscopy was conducted (Figure 3a,d). During annealing, the absorption intensity of the control sample rose sharply and reached its maximum value at 10.08 s, indicative of the rapid formation of the black perovskite phase. In contrast, the EAH-treated film required 21.79 s to reach its maximum absorbance. The delayed crystallization process induced by the strong EAH–perovskite interaction favors the formation of high-quality perovskite films with improved crystal orientation [47, 48].

The influence of EAH molecules on the wettability and surface morphology of the perovskite film was further investigated. Glass/ITO/NiO_x/Me-4PACz films were prepared for contact angle measurements of the perovskite precursor solution with and without EAH. As depicted in Figure S3, the introduction of EAH decreased the contact angle from 36.34° (control) to 28.45°, indicating improved wettability. Enhanced wettability enabled more uniform spreading of the perovskite precursor solution, leading to the formation of a homogeneous and compact film. This observation is supported by surface and cross-sectional scanning electron microscopy (SEM) analyses. Compared with the control films, the EAH-treated film exhibited a substantial increase in average grain size from 437 to 554 nm, with grains exceeding 1 μm and fewer pinholes (Figure 3b,e). The reduced GBs and voids contributed to lower defect density and suppressed nonradiative recombination. Moreover, the cross-section morphology revealed a highly ordered vertical structure in the EAH-modified film (Figure S4). Atomic force microscopy (AFM) measurements confirmed a similar trend: the root-mean-square (RMS) roughness decreased from 16.80 (control) to 14.83 nm upon EAH treatment (Figure 3c,f), demonstrating a smoother surface. Larger, pinhole-free grains and a smoother surface reduce the density of recombination-active GBs and minimize leakage currents, thereby facilitating charge transport in the perovskite layer and ultimately enhancing the performance of PSCs [49]. The crystalline quality was further assessed by X-ray diffraction (XRD) tests. The EAH treatment film exhibited stronger diffraction intensity and a narrower full width at half maximum (FWHM) of 0.326° for the (100) plane compared with the control film (Figure 3g,h), indicating superior crystallinity and fewer defects. A slight shift of the (100) diffraction peak toward higher angles was observed for the EAH-treated film, which can be attributed to the incorporation of Cl^- ions (originating from EAH) into the perovskite lattice [50]. The optical properties of perovskite films were further examined by UV–vis absorption spectroscopy (Figure 3i).

1864564x, 2026, 3, Downloaded from https://chemistry-europe.onlinelibrary.wiley.com/doi/10.1002/cssc.202502563 by RENMIN UNIVERSITY OF CHINA NON-EAL ACCOUNT, Wiley Online Library on [04/11/2026]. See the Terms and Conditions (https://onlinelibrary.wiley.com/terms-and-conditions) on Wiley Online Library for rules of use; OA articles are governed by the applicable Creative Commons License

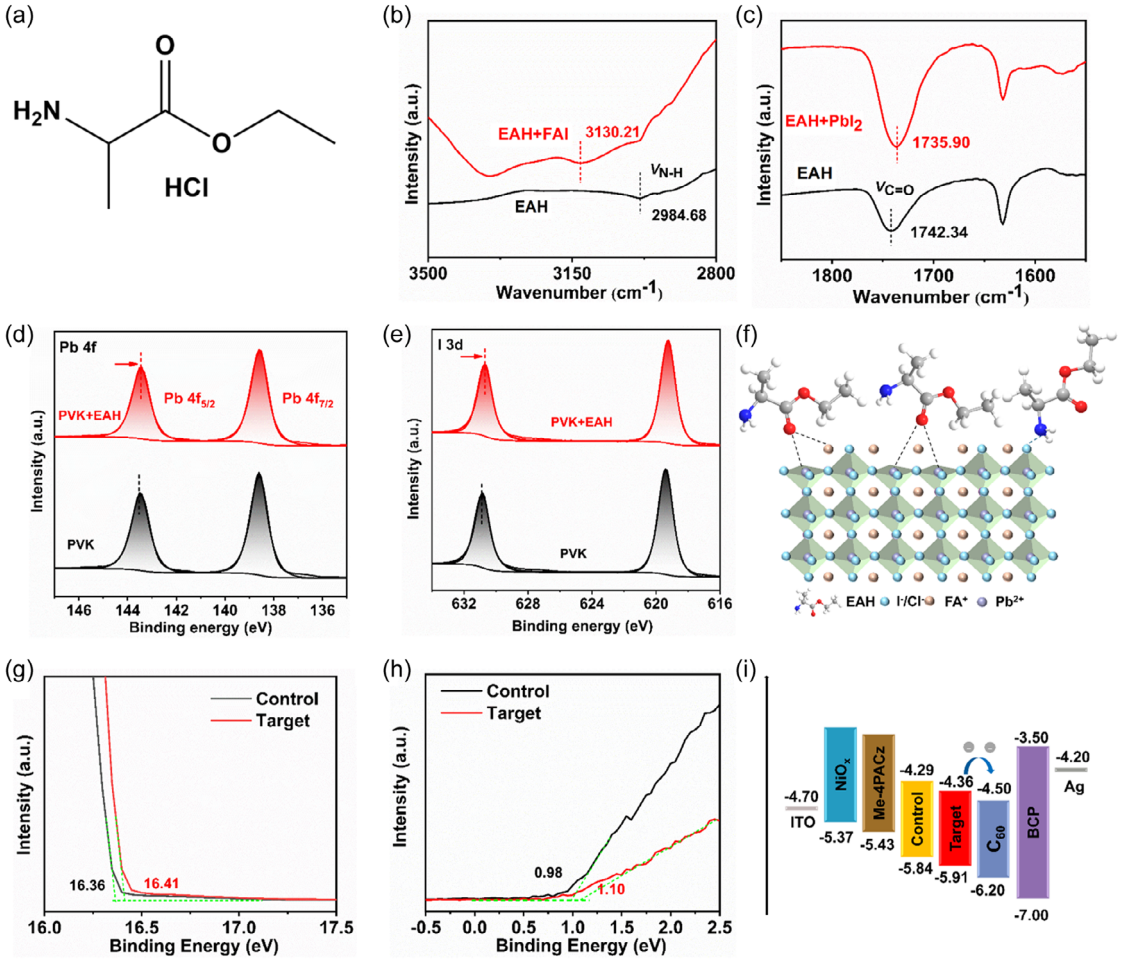


FIGURE 2 | (a) Chemical structure of the EAH molecule. FTIR spectra of (b) pure EAH and FAI + EAH, and (c) pure EAH and PbI_2+ EAH. XPS spectra of (d) Pb 4f, (e) I 3d for control and EAH-treated perovskite films. (f) Schematic illustration of EAH-induced defect passivation in perovskite films. UPS spectra of control and EAH-treated perovskite films in the (g) cutoff and (h) onset regions. (i) Schematic energy-level diagram of perovskites with and without treatment.

Benefiting from the enlarged grain size and reduced defect density, the EAH-modified film exhibits enhanced light-harvesting capability, which contributes to improved optoelectronic performance of the device.

PSCs with p-i-n structure (ITO/NiO_x/Me-4PACz/perovskite/C_{60}/BCP/Ag) were fabricated to evaluate the impact of EAH modification on device performance. The concentration of EAH additive was optimized, and 0.5 mg mL^{-1} as the optimal value for the PCE of devices (Figure S5, Table S1). Figure 4a,b displays the current density–voltage (J–V) curves of the best-performing devices. The control device achieved a PCE of 20.06%, with a short-circuit current density (J_{SC}) of 24.07 mA cm^{-2}, an open-circuit voltage (V_{OC}) of 1.087 V, and a fill factor (FF) of 76.71%. In contrast, the EAH-treated device demonstrates a significant enhanced PCE of 22.58%, along with a J_{SC} of 24.95 mA cm^{-2}, a V_{OC} of 1.122 V, and an FF of 80.65%. The simultaneous improvements in J_{SC}, V_{OC}, and FF demonstrate that EAH effectively enhances charge transport and suppresses nonradiative recombination by optimizing energy-level alignment and passivating bulk defects. Statistical analysis of 24 individual devices further confirmed the reproducibility of this enhancement, with average PCEs of 19.64% ± 0.25% and 22.14% ± 0.22% for the control and EAH-modified PSCs, respectively (Figure S6, Table 1). The external quantum efficiency (EQE) spectra in Figure 4c further validated these results, showing integrated J_{SC} values of 22.98 and 24.00 mA cm^{-2} for the control and EAH-treated devices, respectively, consistent with the J–V results. Device stability was also systematically evaluated. As illustrated in Figure 4d, unencapsulated EAH-treated devices retained 95.1% of their initial PCE after 1368 h of storage in an N_2 glovebox at 25°C, while control PSC maintained only 84.8% under the same conditions. Under continuous thermal aging at 65°C for 1272 h, the EAH-modified devices maintained 94.1% of their initial PCE, compared to 78.3% for the control. Finally, we traced the unencapsulated devices' efficiency under ambient air (20°C, 45 ± 5% RH) for 984 h. The EAH-treated devices retained 76.2% of their initial PCE, while the control devices dropped to only 61.7% (Figure S7). These results clearly demonstrated that the EAH passivation strategy significantly improves multienvironmental stability by passivating bulk defects and promoting high-quality perovskite crystallization.

To gain deeper insight into the correlation between defect states and device performance, comprehensive photoelectrochemical characterizations were conducted. The dark J–V curves (Figure 4e) revealed that the EAH-modified device showed a lower reverse saturation current than the control, confirming that bulk defects

1864564x, 2026, 3, Downloaded from https://chemistry-europe.onlinelibrary.wiley.com/doi/10.1002/cssc.202502563 by RENMIN UNIVERSITY OF CHINA NON-EAL ACCOUNT, Wiley Online Library on [04/11/2026]. See the Terms and Conditions (https://onlinelibrary.wiley.com/terms-and-conditions) on Wiley Online Library for rules of use; OA articles are governed by the applicable Creative Commons License

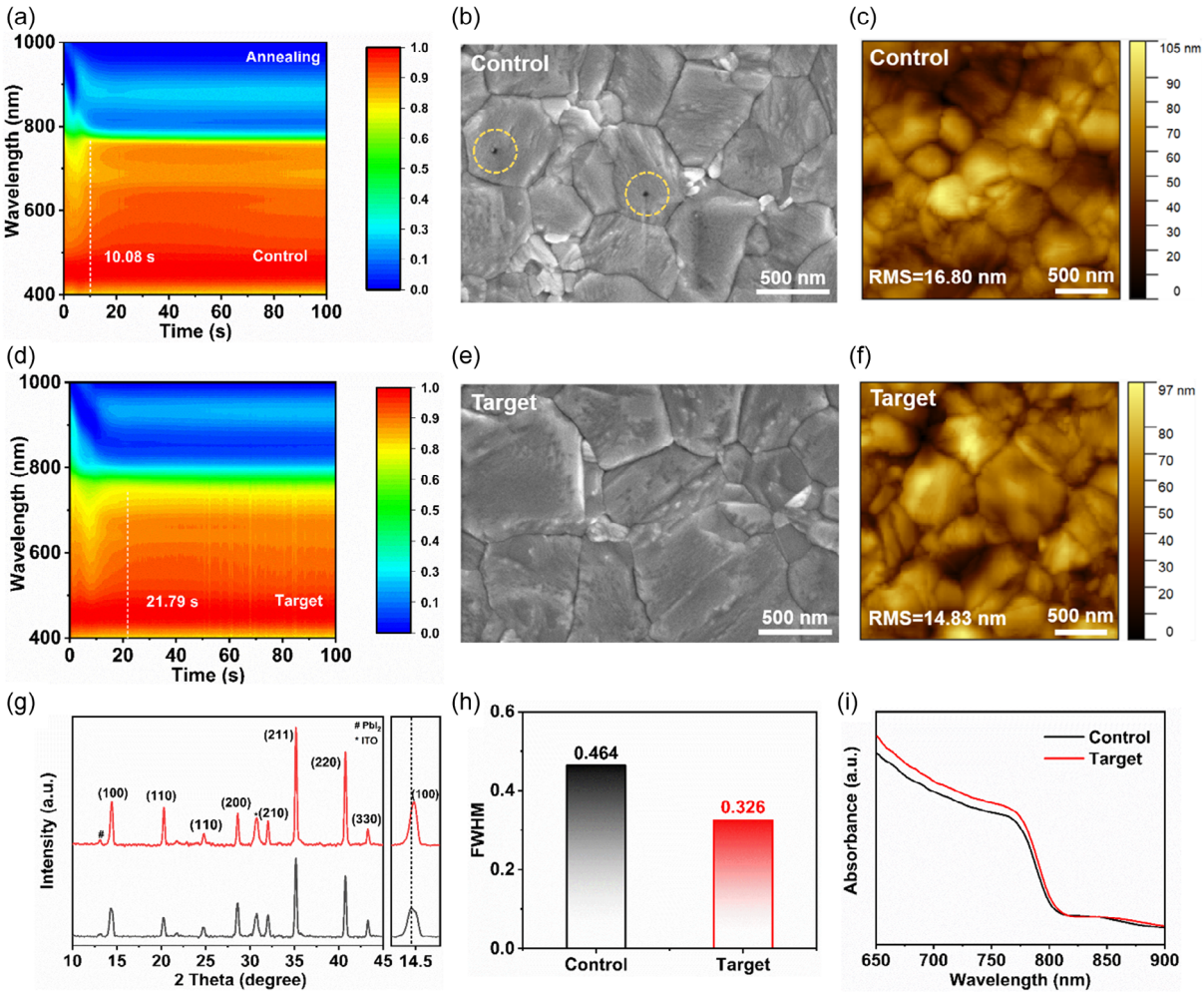


FIGURE 3 | In situ UV–vis spectra tracking the formation of (a) control and (d) target films during the first 100 s of annealing. Top-view SEM images of (b) the control and (e) EAH-treated perovskite films. AFM images of (c) the control and (f) EAH-treated perovskite films. (g) XRD patterns and magnified (100) diffraction peaks of the perovskite films with and without EAH. (h) The FWHM values of the (100) diffraction peaks of the control and EAH-treated perovskite films. (i) UV–vis absorption spectra of the perovskite films with and without EAH.

are effectively passivated by EAH [51]. To quantitatively evaluate the trap density (N_t), electron-only devices with the structure ITO/SnO_2/perovskite/C_{60}/BCP/Ag were fabricated for space-charge-limited current (SCLC) measurements. As shown in Figure 4f, the trap-filled limit voltage (V_{TFL}) decreased from 0.817 V for the control device to 0.677 V for the EAH device. The N_t was calculated using $N_t = \frac{2\varepsilon\varepsilon_0 V_{TFL}}{eL^2}$, where ε and ε_0 are the relative dielectric constant of perovskite (46.5) and the vacuum permittivity, respectively [52], e is the elementary charge, and L is the thickness of the perovskite film (750 nm).The N_t values for the control and EAH-treated device were 7.47×10^{15} and 6.19×10^{15} cm^{-3}, respectively (Table S2), demonstrating a clear reduction in trap density after EAH modification. To further elucidate the recombination behavior, light-intensity-dependent V_{OC} measurements were performed. The slope of V_{OC} versus the logarithm of light intensity yielded ideality factors (n) of 1.64 and 1.29 for the control and EAH-treated devices, respectively (Figure 4g), indicating that EAH effectively suppressed trap-assisted recombination [53, 54]. Electrochemical impedance spectroscopy (EIS) was also used to evaluate charge transport and recombination resistance. Nyquist plot fitting based on the equivalent circuit model revealed an increase in recombination resistance (R_{rec}) from 9245 to 12,471 Ω upon EAH treatment (Figure 4h, Table S3), suggesting inhibited charge recombination and enhanced carrier transport efficiency [55]. Furthermore, Mott–Schottky analysis demonstrated an enhancement in the built-in potential (V_{bi}) from 0.86 V (control) to 0.92 V after EAH modification (Figure 4i), confirming a stronger internal electric field that facilitates photogenerated carrier separation and transport, thereby contributing to the increased V_{OC} and overall device performance [56]. The hysteresis behavior was also analyzed by measuring the J–V characteristics at different scan rates (0.01–30 V/s). The EAH-passivated PSCs exhibited significantly lower hysteresis factors (HF) (Figure S8), indicative of suppressed ion migration and improved operational stability [57, 58]. Collectively, these results confirmed that EAH modification effectively reduced trap-state density, suppressed nonradiative recombination, enhanced carrier transport, and ultimately improved the efficiency and stability of PSCs.

To investigate the influence of EAH modification on the recombination characteristics and carrier transport behavior, steady-state photoluminescence (PL) and time-resolved PL (TRPL) measurements were performed on glass/perovskite films

1864564x, 2026, 3, Downloaded from https://chemistry-europe.onlinelibrary.wiley.com/doi/10.1002/cssc.202502563 by RENMIN UNIVERSITY OF CHINA NON-EAL ACCOUNT, Wiley Online Library on [04/11/2026]. See the Terms and Conditions (https://onlinelibrary.wiley.com/terms-and-conditions) on Wiley Online Library for rules of use; OA articles are governed by the applicable Creative Commons License

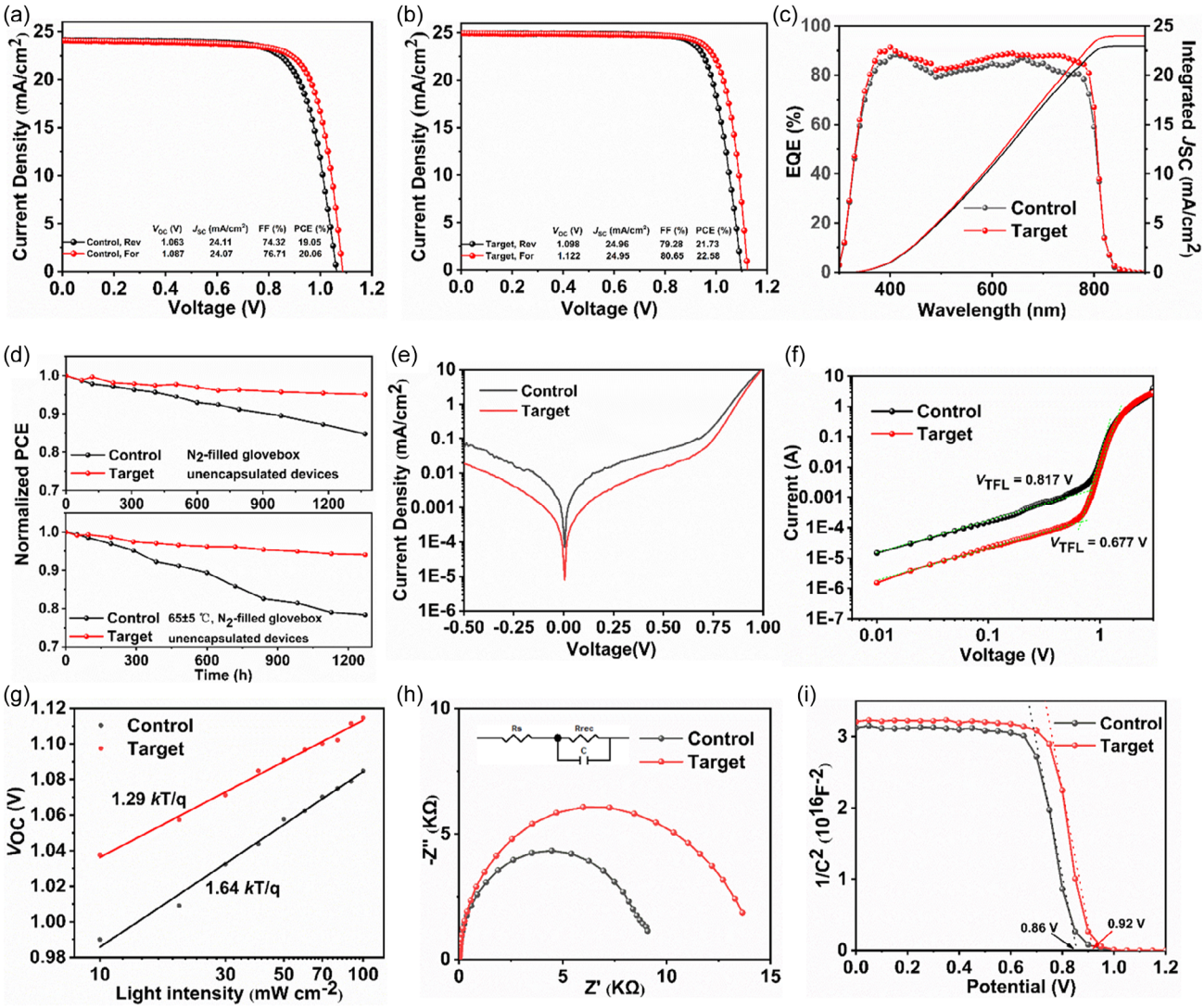


FIGURE 4 | (a,b) Champion *J–V* curves of the PSCs: (a) without and (b) with EAH treatment. (c) EQE spectra and integrated J_{SC} curves. (d) Normalized PCE of the inverted PSCs with and without EAH under storage and thermal aging at 65°C in a nitrogen-filled glovebox. (e) Dark *J–V* curves characteristics. (f) SCLC curves of electron-only devices. (g) V_{OC} versus light intensity, (h) Nyquist plots, and (i) Mott–Schottky curves of the control and EAH-modified devices.

TABLE 1 | Average photovoltaic parameters of inverted PSCs from 24 devices.

Sample	V_{OC}, V	J_{SC}, mA/cm²	FF, %	PCE, %
Control	1.069 ± 0.009	23.80 ± 0.30	76.32 ± 1.31	19.64 ± 0.25
Target	1.109 ± 0.007	24.90 ± 0.09	79.88 ± 0.65	22.14 ± 0.22

(Figure 5a,b). The EAH-modified perovskite film exhibited a stronger PL intensity than the control, suggesting enhanced crystal quality and reduced nonradiative recombination. The TRPL decay curves were fitted with a biexponential model to obtain the carrier lifetime parameters. The average carrier lifetime (τ_{ave}) of the EAH-treated film increased to 4.67 μs, compared with 2.98 μs for the control (Table S4), indicating more efficient charge extraction and suppressed trap-assisted recombination. Furthermore, transient photocurrent (TPC) and transient photovoltage (TPV) analyses were conducted to elucidate charge transport kinetics. After EAH modification, the TPC decay time decreased from 0.671 to 0.514 μs, while the TPV decay time increased from 53.07 to 116.53 μs (Figure 5c,d). These results confirmed accelerated charge collection and reduced carrier recombination in the EAH-modified device [59]. Additionally, open-circuit voltage decay (OCVD) measurements were carried out by monitoring V_{OC} decay under dark conditions after light irradiation [60–62]. As shown in Figure S9, the EAH-treated PSCs exhibited a slower V_{OC} decay compared to the control, further confirming the suppression of free-carrier recombination in the perovskite bulk. Overall, these results demonstrated that the introduction of EAH effectively enhanced charge-carrier transport, suppressed nonradiative recombination, and promoted improved optoelectronic performance in PSCs.

1864564x, 2026, 3, Downloaded from https://chemistry-europe.onlinelibrary.wiley.com/doi/10.1002/cssc.202502563 by RENMIN UNIVERSITY OF CHINA NON-EAL ACCOUNT, Wiley Online Library on [04/11/2026]. See the Terms and Conditions (https://onlinelibrary.wiley.com/terms-and-conditions) on Wiley Online Library for rules of use; OA articles are governed by the applicable Creative Commons License

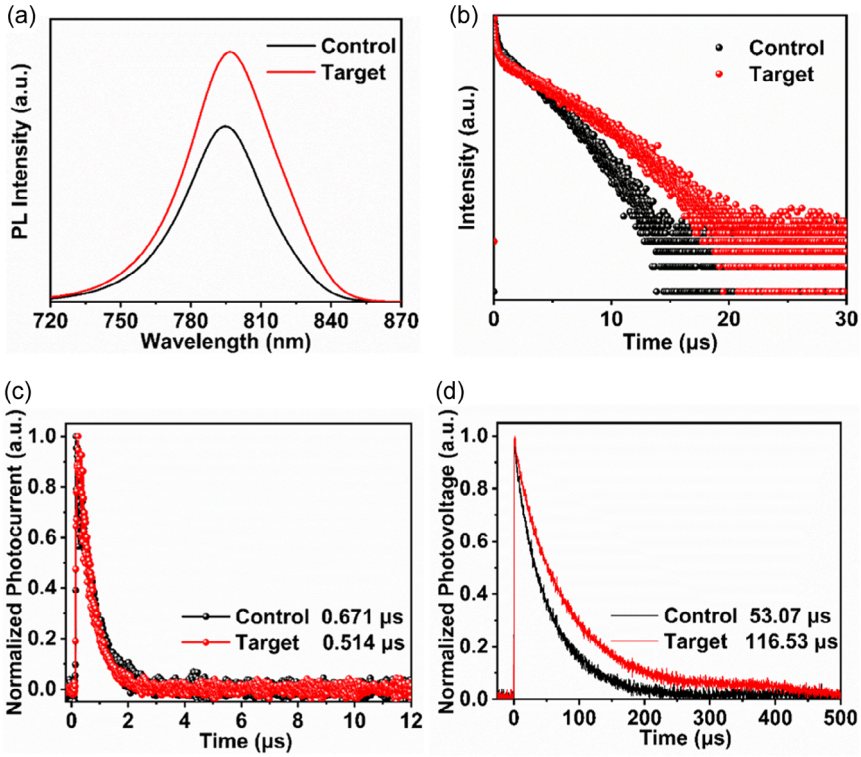


FIGURE 5 | (a) Steady-state PL and (b) time-resolved PL spectra of the perovskite films with and without the EAH incorporation. (c) TPC and (d) TPV curves of control and EAH PSCs.

3 | Conclusion

In summary, we demonstrated an effective strategy that integrates the Perovskite-R1 LLM to efficiently identify a high-performance precursor additive, EAH. The incorporation of EAH effectively passivated bulk defects and modulated the crystallization kinetics of the perovskite layer through strong interactions between its functional groups and perovskite components, resulting in enlarged grain sizes and a smoother film surface. Simultaneously, EAH improved energy-level alignment at the interface of the perovskite layer and the hole transport layer, enhanced charge-carrier transport, and suppressed nonradiative recombination. Consequently, the EAH-modified device achieved a champion PCE of 22.58%. Moreover, the interaction between EAH and the perovskite components helped stabilize the perovskite structure, maintaining 95.1% and 94.1% of their initial efficiency after 1368 h of storage and 1272 h of thermal aging at 65°C, respectively. In summary, the EAH molecule's structural properties are highly consistent with our preset additive standards, with its performance optimization also meeting our expectations, thereby demonstrating the effectiveness and reliability of our adopted LLM-assisted additive selection approach. This work highlights the potential of LLMs in accelerating materials discovery and provides a promising paradigm for intelligent additive screening and optimization in perovskite photovoltaic technology.

Acknowledgments

This study was supported by the National Energy Green Hydrogen Refining Research & Development Center, Beijing Natural Science Foundation (2252009), Beijing Natural Science Foundation (no. Z250005), and the National Natural Science Foundation of China (no. 62476278, no. 12434009).

Funding

This work was supported by the National Energy Green Hydrogen Refining Research & Development Center, Beijing Natural Science Foundation (2252009 and Z250005), and the National Natural Science Foundation of China (62476278 and 12434009).

Conflicts of Interest

The authors declare no conflicts of interest.

Data Availability Statement

The data that support the findings of this study are available on request from the corresponding author. The data are not publicly available due to privacy or ethical restrictions.

References

1. T. W. Duan, S. You, M. Chen, et al., "Chiral-Structured Heterointerfaces Enable Durable Perovskite Solar Cells," *Science* 384 (2024): 878.

2. W. Zhang, X. Guo, Z. Cui, et al., "Strategies for Improving Efficiency and Stability of Inverted Perovskite Solar Cells," *Advanced Materials* 36 (2024): 2311025.

3. D. P. McMeekin, G. Sadoughi, W. Rehman, et al., "Amixed-Cation Lead Mixed-Halide Perovskite Absorber for Tandem Solar Cells," *Science* 351 (2016): 151.

4. S. D. Stranks, G. E. Eperon, G. Grancini, et al., *Science* 342 (2013): 341–344.

18645643x, 2026, 3, Downloaded from https://chemistry-europe.onlinelibrary.wiley.com/doi/10.1002/cssc.202502563 by RENMIN UNIVERSITY OF CHINA NON-EAL ACCOUNT, Wiley Online Library on [04/11/2026]. See the Terms and Conditions (https://onlinelibrary.wiley.com/terms-and-conditions) on Wiley Online Library for rules of use; OA articles are governed by the applicable Creative Commons License

5. J. H. Noh, S. H. Im, J. H. Heo, T. N. Mandal, and S. I. Seok, "Chemical Management for Colorful, Efficient, and Stable Inorganic–Organic Hybrid Nanostructured Solar Cells," *Nano Letters* 13 (2013): 1764.

6. D. Shi, V. Adinolfi, R. Comin, et al., "Low Trap-State Density and Long Carrier Diffusion in Organolead Trihalide Perovskite Single Crystals," *Science* 347 (2015): 519.

7. Q. Dong, Y. Fang, Y. Shao, P. Mulligan, J. Qiu, L. Cao, and J. Huang, "Electron-Hole Diffusion Lengths >175 mm in Solution-Grown $CH_3NH_3PbI_3$ Single Crystals," *Science* 347 (2015): 967.

8. A. Kojima, K. Teshima, Y. Shirai, and T. Miyasaka, "Organometal Halide Perovskites as Visible-Light Sensitizers for Photovoltaic Cells," *Journal of the American Chemical Society* 131 (2009): 6050.

9. NREL, "*Best Research-Cell Efficiencies*," accessed November 2025, https://www.nrel.gov/pv/assets/pdfs/best-research-cell-efficiencies.pdf.

10. Y. Tong, A. Najar, L. Wang, et al., "Wide-Bandgap Organic–Inorganic Lead Halide Perovskite Solar Cells," *Advancement of Science* 9 (2022): 2105085.

11. J.-W. Lee, S.-H. Bae, Y.-T. Hsieh, N. De Marco, M. Wang, P. Sun, and Y. Yang, "A Bifunctional Lewis Base Additive for Microscopic Homogeneity in Perovskite Solar Cells," *Chem* 3 (2017): 290.

12. D. Bi, C. Yi, J. Luo, et al., "Polymer-Templated Nucleation and Crystal Growth of Perovskite Films for Solar Cells with e Ciency Greater than 21%," *Nature Energy* 1 (2016): 16142.

13. D. P. McMeekin, P. Holzhey, S. O. Furer, et al., "Intermediate-Phase Engineering via Dimethylammonium Cation Additive for Stable Perovskite Solar Cells," *Nature Materials* 22 (2023): 73.

14. L. Bi, Q. Fu, Z. Zeng, et al., "Deciphering the Roles of MA-Based Volatile Additives for α-$FAPbI_3$ to Enable Efficient Inverted Perovskite Solar Cells," *Journal of the American Chemical Society* 145 (2023): 5920.

15. X. Li, M. I. Dar, C. Yi, et al., "Improved Performance and Stability of Perovskite Solar Cells by Crystal Crosslinking with Alkylphosphonic Acid ω-Ammonium Chlorides," *Nature Chemistry* 7 (2015): 703.

16. H. Min, M. Kim, S.-U. Lee, et al., "Efficient, Stable Solar Cells by Using Inherent Bandgap of a-Phase Formamidinium Lead Iodide," *Science* 366 (2019): 749.

17. J. Chen and N.-G. Park, "Causes and Solutions of Recombination in Perovskite Solar Cells," *Advanced Materials* 31 (2019): 1803019.

18. S. Bai, P. Da, C. Li, et al., "Planar Perovskite Solar Cells with Long-Term Stability Using Ionic Liquid Additives," *Nature* 571 (2019): 245.

19. J. Qu, W. Zhang, Y. Chen, et al., "Multifunctional Amine Salt Additive for Enhancing the Performance of Perovskite and Perovskite/Silicon Tandem Solar Cells," *Chemical Engineering Journal* 515 (2025): 163967.

20. H. Lv, J. Liu, P. Wang, et al., "A Dual-Functional Coordination Additive for Defect Passivation and Large-Grain Formation in Perovskite Film," *Advanced Functional Materials* 35 (2025): e10831.

21. J. Zhou, J. Lv, L. Tan, et al., "High-Efficiency Large-Area Perovskite Solar Cells via a Multifunctional Crystallization Regulating Passivation Additive," *Advanced Materials* 37 (2025): 2502916.

22. Y. F. Shao, S. L. Wang, T. Luo, et al., "Multi-Functional Interface Engineering for Monolithic Perovskite/Perovskite/Crystalline Silicon Triple-Junction Tandem Solar Cells," *Chemsuschem* 18 (2025): e202402680.

23. J. Z. Liu, C. B. Ai, C. R. Hu, B. Cheng, and J. J. Zhang,, "Accelerated Interfacial Electron Transfer in Perovskite Solar Cell by Ammonium Hexachlorostannate Modification and fs-TAS Investigation," *Acta Physico-Chimica Sinica* 40 (2024): 2402006.

24. Y. Pu, Z. Dai, Y. Zhou, et al., "Data-Driven Molecular Encoding for Efficient Screening of Organic Additives in Perovskite Solar Cells," *Advanced Functional Materials* 36 (2025): e06672.

25. K. Choudhary and B. DeCost, "Atomistic Line Graph Neural Network for Improved Materials Property Predictions," *Npj Computational Materials* 7 (2021): 185.

26. C. Chen and S. P. Ong, "A Universal Graph Deep Learning Interatomic Potential for the Periodic Table ," *Nature Computational Science* 2 (2022): 718.

27. S. Kim, J. Noh, G. H. Gu, A. Aspuru-Guzik, and Y. S. Jung, "Generative Adversarial Networks for Crystal Structure Prediction," *ACS Central Science* 6 (2020): 1412.

28. M. Popova, O. Isayev, and A. Tropsha, "Deep Reinforcement Learning for De Novo Drug Design," *Science Advances* 4 (2018): eaap7885.

29. T. Xie and J. C. Grossman, "Crystal Graph Convolutional Neural Networks for an Accurate and Interpretable Prediction of Material Properties," *Physical Review Letters* 120 (2018): 145301.

30. D. A. Boiko, R. Macknight, B. Kline, and G. Gomes, "Autonomous Chemical Research with Large Language Models," *Nature* 624 (2023): 570.

31. K. M. Jablonka, Q. X. Ai, A. Al-Feghali, et al., "14 Examples of How LLMs Can Transform Materials Science and Chemistry: A Reflection on a Large Language Model Hackathon," *Digital Discovery* 2 (2023): 1233.

32. A. M. Bran, S. Cox, O. Schilter, C. Baldassari, A. D. White, and P. Schwaller, "Augmenting Large Language Models with Chemistry Tools," *Nature Machine Intelligence* 6 (2024): 525.

33. V. Bagal, R. Aggarwal, P. K. Vinod, and U. D. Priyakumar, "MolGPT: Molecular Generation Using a Transformer-Decoder Model," *Journal of Chemical Information and Modeling* 62 (2022): 2064.

34. L. M. Antunes, K. T. Butler, and R. Grau-Crespo, "Crystal Structure Generation with Autoregressive Large Language Modeling," *Nature Communications* 15 (2024): 10570.

35. X.-Q. Han, X.-D. Wang, M.-Y. Xu, et al., "AI-Driven Inverse Design of Materials: Past, Present, and Future," *Chinese Physics Letters* 42 (2025): 027403.

36. X.-D. Wang, Z.-R. Chen, P.-J. Guo, Z.-F. Gao, C. Mu, and Z.-Y. Lu, arXiv preprint, 2025, https://doi.org/10.48550/arXiv.2507.16307.

37. L. Zhu, H. Cao, C. Xue, et al., "Unveiling the Additive-Assisted Oriented Growth of Perovskite Crystallite for High Performance Light Emitting Diodes," *Nature Communications* 12 (2021): 5081.

38. Y. Li, Z. Zhang, Y. Cai, et al., "Synergistic Isothiourea–Guanidine Additive for Achieving Stable Perovskite Solar Cells with a High Certified Quasi-Steady-State Output," *Advanced Materials* (2025): e14903.

39. X. Zhao, R. Luo, C. Yu, et al., "Hydrogen-Bond-Based Polymer-Ammonium Intermediates Induced Buried Interface Engineering for High-Performance Inverted Perovskite Solar Cells," *Advanced Functional Materials* 34 (2024): 2307568.

40. C. Li, N. Zhang, and P. Gao, "Lessons Learned: How to Report XPS Data Incorrectly about Lead-Halide Perovskites," *Materials Chemistry Frontiers* 7 (2023): 3797.

41. B. Jiao, L. Tan, Y. Ye, et al., "One-Stone-Two-Birds: Over 26% Efficiency in Perovskite Solar Cells via Synergistic Crystallization & Interface Regulation," *Energy & Environmental Science* 18 (2025): 5437.

42. J. Euvrard, Y. Yan, and D. B. Mitzi, "Electrical Doping in Halide Perovskites," *Nature Reviews. Materials* 6 (2021): 531.

43. N. Liu and C. Yam, "First-Principles Study of Intrinsic Defects in Formamidinium Lead Triiodide Perovskite Solar Cell Absorbers," *Physical Chemistry Chemical Physics* 20 (2018): 6800.

44. X. Hu, J. Li, C. Wang, et al., "Antimony Potassium Tartrate Stabilizes Wide-Bandgap Perovskites for Inverted 4-T All-Perovskite Tandem Solar Cells with Efficiencies over 26%," *Nano-Micro Letters* 15 (2023): 103.

45. Y. Zheng, X. Wu, J. Liang, et al., "Downward Homogenized Crystallization for Inverted Wide-Bandgap Mixed-Halide Perovskite Solar Cells with 21% Efficiency and Suppressed Photo-Induced Halide Segregation," *Advanced Functional Materials* 32 (2022): 2200431.

1864564x, 2026, 3, Downloaded from https://chemistry-europe.onlinelibrary.wiley.com/doi/10.1002/cssc.202502563 by RENMIN UNIVERSITY OF CHINA NON-EAL ACCOUNT, Wiley Online Library on [04/11/2026]. See the Terms and Conditions (https://onlinelibrary.wiley.com/terms-and-conditions) on Wiley Online Library for rules of use; OA articles are governed by the applicable Creative Commons License

46. S. Xiong, Z. Hou, S. Zou, et al., "Direct Observation on p- to n-Type Transformation of Perovskite Surface Region during Defect Passivation Driving High Photovoltaic Efficiency," *Joule* 5 (2021): 467.

47. F. Qiu, H. Cheng, P. Mao, et al., "Unifying Crystal Growth and Defect Passivation in Photovoltaic Perovskites: The Impact of Molecular Coordinating Strength," *Acs Energy Letters* 9 (2024): 1115.

48. Y. Peng, Y. Chen, Y. Shen, et al., "Heterogeneous-Nucleation and Epitaxial-Growth of Perovskite Enabled by Delafossite-Type HoleTransport Materials for High-Performance Solar Cells," *Advanced Functional Materials* (2025): e21121.

49. M. W. Hao and Y. Y. Zhou, "Grain-Boundary Grooves in Perovskite Solar Cells," *Joule* 8 (2024): 913.

50. Z. Bing, J. Huang, and F. Li, "Benzamidine Derivative as a Multifunctional Additive in Pb−Sn Perovskite Solar Cells," *Journal of Physical Chemistry Letters* 16 (2025): 10071.

51. O. Omelianovych, S. Sandhu, M. A. Ewusi, et al., "Stable and Efficient Perovskite Solar Cells by Controlling the Crystal Growth via Introduction of Plasmonic TiN Nanoparticles," *Advanced Functional Materials* 34 (2024): 2407343.

52. Z. W. Feng, Y. B. Wang, J. Z. Si, et al., "Multi-Site Lead Passivation via Spatial Configuration Modulation of Additives for Efficient Perovskite Solar Cells," *Advanced Energy Materials* 15 (2025): 2502409.

53. Z. Zhang, J. Wang, J. Liang, et al., "Organizing Uniform Phase Distribution in Methylammonium-Free 1.77 eV Wide-Bandgap Inverted Perovskite Solar Cells," *Small* 19 (2023): 2303213.

54. C. Zhu, X. Niu, Y. Fu, et al., "Strain Engineering in Perovskite Solar Cells and Its Impacts on Carrier Dynamics," *Nature Communications* 10 (2019): 815.

55. J. Liu, J. Chen, P. Xu, et al., "Dual Role of Rapid Transport and Efficient Passivation in Inverted Methylammonium-Free Perovskite Solar Cells Utilizing a Self-Assembled Porous Insulating Layer," *Advanced Energy Materials* 14 (2024): 2303092.

56. J. Bisquert and A. Guerrero, "Dynamic Instability and Time Domain Response of a Model Halide Perovskite Memristor for Artificial Neurons," *journal of Physical Chemistry Letters* 13 (2022): 3789.

57. S. Shah, F. Yang, E. Koehnen, et al., "Impact of Ion Migration on the Performance and Stability of Perovskite-Based Tandem Solar Cells," *Advanced Energy Materials* 14 (2024): 2400720.

58. F. Lou, S. Yuan, X. Wang, et al., "Distinguishing the Migration Time Scale of Ion Species in Perovskite Solar Cells," *Chemical Physics Letters* 796 (2022): 139570.

59. H. Zhao, J. Ding, X. Liu, et al., "Intermolecular Interaction Induced Synergistic Uniform Passivation of Grain Boundary Multiple Defects Enables High-Performance Inverted Perovskite Solar Cells," *Advanced Functional Materials* (2025): 2504424.

60. G. A. Sepalage, S. Meyer, A. Pascoe, et al., "Iodide as Hole-Conductor in Planar Perovskite Solar Cells: Probing the Origin of *J–V* Hysteresis," *Advanced Functional Materials* 25 (2015): 5650.

61. L. Bertoluzzi, R. S. Sanchez, L. Liu, et al., "Cooperative Kinetics of Depolarization in $CH_3NH_3PbI_3$ Perovskite Solar Cells," *Energy & Environmental Science* 8 (2015): 910.

62. Y. Liu, N. Borodinov, L. Collins, et al., "Role of Decomposition Product Ions in Hysteretic Behavior of Metal Halide Perovskite," *ACS Nano* 15 (2021): 9017.

Supporting Information

Additional supporting information can be found online in the Supporting Information section. **Supporting Fig. S1:** FTIR spectra of pure EAH and PbI_2+ EAH. **Supporting Fig. S2:** FTIR spectra of pure EAH and FAI+ EAH. **Supporting Fig. S3:** Contact angles of the control and EAH-treated perovskite precursor solutions on the NiO_x/Me-4PACz HTL. **Supporting Fig. S4:** Cross-section SEM images for the control and EAH-treated perovskite films. **Supporting Fig. S5:** *J-V* curves of PSCs with different amounts of EAH additives. **Supporting Fig. S6:** (a) PCE, (b) J_{SC}, (c) FF, (d) V_{OC} statistic diagrams obtained from 24 devices with and without EAH. **Supporting Fig. S7:** Normalized PCE of the unencapsulated devices with and without EAH aged in air atmosphere with $RH = 45 \pm 5\%$. **Supporting Fig. S8:** Hysteresis factor dependence on voltage scan rates in devices with and without EAH. **Supporting Fig. S9:** OCVD profiles of the devices with and without EAH. **Supporting Table S1:** Photovoltaic parameters of the PSCs with different EAH additive concentrations. **Supporting Table S2:** N_t calculated from the I−V curves of SCLC measurements for the perovskite film with and without EAH. **Supporting Table S3:** The fitting parameters of Nyquist plots for the control and target PSCs. **Supporting Table S4:** TRPL fitting parameters.

1864564x, 2026, 3, Downloaded from https://chemistry-europe.onlinelibrary.wiley.com/doi/10.1002/cssc.202502563 by RENMIN UNIVERSITY OF CHINA NON-EAL ACCOUNT, Wiley Online Library on [04/11/2026]. See the Terms and Conditions (https://onlinelibrary.wiley.com/terms-and-conditions) on Wiley Online Library for rules of use; OA articles are governed by the applicable Creative Commons License